Geophys. J. Int. (2002) **149,** 134–148

Modelling and imaging the Moho transition: the case of the southern Urals

R. Carbonell, J. Gallart and A. Pérez-Estaún

Dept. Geofisica, C.S.I.C.-Inst. Ciencias de la Tierra "Jaume Alert", 08028 *Barcelona, Spain. E-mail: rcarbo@ija.csic.es*

Accepted 2001 October 10. Received 2001 September 17; in original form 2000 May 16

SUMMARY

Synthetic seismic modelling is used to test different possible structures and forming processes of the lower crust and Moho. One and two dimensional synthetic seismic modelling of the Moho reflection is carried out to constrain the internal structure of a crust–mantle transition. A reflectivity algorithm was used to calculate the synthetic seismograms for models of the crust–mantle transition consisting of gradient zones and layered sequences. The synthetic seismograms for models consisting of laterally variable velocity structure were calculated by an explicit finite difference wave equation algorithm. The laterally heterogeneous transition models can be achieved by assuming a Moho with different degrees of variable topography or laterally discontinuous layering. The effects of a low velocity surface cover on the seismic signature of deep signals is also analysed. The seismic modelling coupled with stacked images of wide-angle seismic reflection data constrain the case history of the Moho transition beneath the southern Urals. A smooth gradational crust–mantle transition (gradient velocity–depth function) does not predict the seismic features observed in the shot records. The coda of the *PmP* and the amplitude behaviour of this phase with offset are modelled with a 6 km thick transition zone which consists of approximately 600 m thick, laterally variable layers with a bimodal velocity distribution. The horizontal component stacks of the wide-angle data feature arcuate events suggesting boudin like structures or a boundary with topographic relief. High amplitude sub-Moho reflections support that the structural complexity of the crust–mantle transition can be followed to the upper mantle suggesting eastward dipping structures indicating, either, remnants of an old subduction zone, trapped crustal material within the mantle, or active crust–mantle interactions.

Key words: Moho discontinuity, seismic modelling, synthetic seismograms.

1 INTRODUCTION

The detailed structure of the Moho has been one of the most important targets in Earth Sciences since its description by Mohorovicić (1910). Seismic refraction and reflection techniques have provided relatively high resolution images of the lower crust and upper mantle since the late 1970's Oliver (1982). The detailed architecture of the crust–mantle transition is the most significant asset in unravelling the lithospheric processes that are involved in extension and in collision zones and provide key knowledge in processes like crustal growth, accretion, delamination, etc. (Hale & Thompson 1982; Larkin *et al.* 1997; Morozov *et al.* 2001; Balling 2000). In recent years, a large number of seismic reflection profiling programmes have provided thousands of kilometres of high resolution images of the deepest parts of the continental crust and of the crust–mantle transition. Such crustal images are of decisive importance for the interpretation of how regional tectonic features and structures observed at the Earth's surface are related to structures at depth, and may be explained in terms of crust-forming tectonic processes (Mooney & Meissner 1992).

The relatively low seismic velocities that characterize the shallow subsurface commonly identified by surface observations can contaminate the seismic signature of deeper structures leading to incorrect geological interpretations. Therefore, it is necessary to investigate the influence of these shallow structures on the waveform of deep seismic reflections. We further discuss the implications of the imaging and modelling strategy on the well studied area of the Southern Urals from which a large amount of geophysical and geological data is available. In particular we use the wide-angle seismic data from the URSEIS'95 multiseismic experiment (Berzin *et al.* 1996; Carbonell *et al.* 1996; Echtler *et al.* 1996; Knapp *et al.* 1996) because the Moho is well imaged by *P* and *S* waves in all the shot gathers. The URSEIS'95 experiment included also Vibroseis and explosive-source normal incidence data. These CMP data sets provided a well constrained high resolution image of the crust (Echtler *et al.* 1996; Knapp *et al.* 1996; Steer *et al.* 1998a). The crustal

thickness and the velocity depth function along the profile were estimated from the wide-angle shot gathers (Carbonell *et al.* 1996, 1998).

The Moho beneath the Southern Urals is a specially intriguing feature, on the CMP sections the Moho appears as a laterally variable structure. It is a sharp event at both ends of the profile, beneath the former EEC margin and beneath the accreted terranes of the Trans-Uralian Zone, and it is not visible beneath the core of the orogen, underneath the Magnitogorsk Volcanic Arc, where the wide-angle data displays a high amplitude *PmP*. Although, published interpretations of the seismic data acquired by the URSEIS'95 lack detailed waveform modelling of the wavefield, the lack of normal incidence reflectivity is taken as evidence for a transitional Moho (gradient velocity model) beneath the Magnitogorsk Volcanic Arc. In this study, the analysis of the synthetic seismograms provide evidence for a complex internal structure of this crust–mantle transition. This feature is further supported by the fan profiles (acquired during the URSEIS'95 experiment) which are also used in composite cross-sections with the wide-angle inline recordings. Additionally, the analysis of the data is extended to the upper mantle by analysing the *P*- and *S*-wave wide-angle stacks. Carbonell *et al.* (1998) described the methodology applied to obtain a *P*-wave wide-angle stack and discussed the shape of the Moho and the thickness of the crust beneath the core of the orogen, using only the *P*-wave wide angle stack. In the present study we present and discuss the shear-wave wide-angle stack images of the Moho beneath a collisional orogen which show evidence for eastward dipping features within the upper mantle.

2 GEOLOGY AND GEOPHYSICS

The descriptions of the geology and tectonic evolution of the Urals, a Palaeozoic orogen, can be found in Navilkin (1960), Ivanov *et al.* (1975), Ivanov & Rusin (1986), Zonenshain *et al.* (1984, 1990), Brown *et al.* (1997, 1998) and Ayarza *et al.* (2000) and references therein. From west to east the most relevant geological features are: the foreland thrust and fold belt developed (East European Craton platform, EEC) on the footwall to the suture, the Main Uralian Fault (MUF), the main suture zone (see Brown *et al.* 1996; Ayarza *et al.* 2000, for details), the Magnitogorsk Volcanic Arc (Seravkin *et al.* 1992; Ivanov & Rusin 1986; Sokolov 1992), the East Uralian Zone, metamorphic Precambrian and Palaeozoic continental crust (Fershtater *et al.* 1997), the Troisk fault and the Trans Uralian Zone (Fig. 1), oceanic derived rocks (ophiolites and island arc rocks).

Relatively low seismic velocity material of a different nature covers the upper most part of the profile. For example: surface exposures of the Magnitogorsk volcanic (Upper Silurian to Upper Devonian volcaniclastics) are covered by Carboniferous sediments, large regions of the Trans-Uralian zone are covered by a thin layer of unconformable Mesozoic–Cenozoic sediments.

The deep crustal structure of the Central and Southern Urals has been the objective of a large amount of seismic experiments including: UWARS (Thouvenot *et al.* 1995) and ESRU (Juhlin *et al.* 1995, 1997) seismic experiments acquired north of Ekaterinbourg, and URSEIS-95 (Echtler *et al.* 1996; Knapp *et al.* 1996; Carbonell *et al.* 1996) acquired across the Southern Urals (Fig. 1). These data support a moderate increase in the crustal thickness beneath the core of the orogen. The URSEIS'95 Vibroseis and explosion CMP sections image a sharp Moho located at 43–45 km depth at the edges of the transect, beneath the EEC and beneath the accreted Siberian terranes of the Trans Uralian Zone. The deep crust beneath the Magnitogorsk Volcanic arc (i.e. root zone) is not well resolved by these normal incidence data (Steer *et al.* 1998a) implying that the Moho is not a distinctive feature in the central part, suggesting a transitional crust–mantle boundary (a gradient zone).

3 WIDE-ANGLE SEISMIC REFLECTION/REFRACTION DATA: FROM REAL DATA TO SYNTHETIC SIMULATIONS

3.1 Processing

The raw wide-angle shot gathers from URSEIS'95 revealed high amplitude seismic phases reflected from the Moho (Carbonell *et al.* 1998, 2000). Following (Carbonell *et al.* 1998) a low frequency wide angle stack of the three component refraction data was obtained. The processing flow included editing the noisy traces, trace amplitude balancing, frequency filtering; aiming to increase the signal-to-noise ratio. The acquisition geometry was used to create common mid-point gathers (CMP) in the same way they are calculated in conventional normal incidence CDP seismic processing. An hyperbolic time shift correction was designed to be applied to the refraction data to flatten the lower crustal and Moho reflections so that the high amplitude *PmP* and *SmS* would stack constructively within a CDP. Further discussion on the processing done to obtain vertical component wide-angle stacks can be found in Carbonell *et al.* (1998). A careful analysis of amplitude spectra revealed that low pass filtering the shot gathers up to 4 or 6 Hz notably increased the lateral correlation of the events in particular the *PmP* and *SmS* phase. An extensive discussion on the frequency content of the data and the design of the appropriate bandpass filtering is given in Carbonell *et al.* (2000).

Although conventional normal move-out (NMO) corrections can be applied to wide-angle seismic data, they are not completely appropriate for the deep events and large offsets characteristic for wide-angle refraction data. Conventional NMO correction applied to far offset wide-angle data results in extremely large stretch of the first arrivals which mask the images. Therefore, a NMO correction without stretch is more suitable for stack processing of wide-angle shot gathers. The time shift is estimated from the traveltime curve for a horizontal reflector, therefore, we use the equation of the hyperbola where the time shift for a trace with offset x (t_x) can be calculated as:

$$t_x = \sqrt{t_0^2 - \frac{x^2}{v^2}} \tag{1}$$

where t_0 is the time for zero offset, x is the offset of the trace, and v is the velocity. In order to obtain an image of the deep crust, Moho and upper mantel, we used the *PmP* as the reference reflection, therefore, t_0 is the normal incidence traveltime (time for offset $x = 0.0$ km) for the Moho and v is the average crustal velocity. Then, eq. (1) represents the time shift that has to be applied to a trace recorded at an offset x in order to flatten the Moho reflection. Eq. (1) has two degrees of freedom. The offset is known, the normal incidence traveltime t_0 and the velocity are two parameters which are not constrained. Nevertheless, for the Moho we have reasonable estimates for all components, which have been computed as ray path averages for each shot using the velocity models determined by Carbonell *et al.* (2000). Thus, they vary from shot to shot. For example, t_0 is within 14–17 s and v ranges from 6.4 to 6.8 km s^{-1} for the vertical components (*PmP*). For the horizontal components t_0 is within 24–29 s and v ranges from 3.7 to 3.9 km s^{-1} (Table 1).

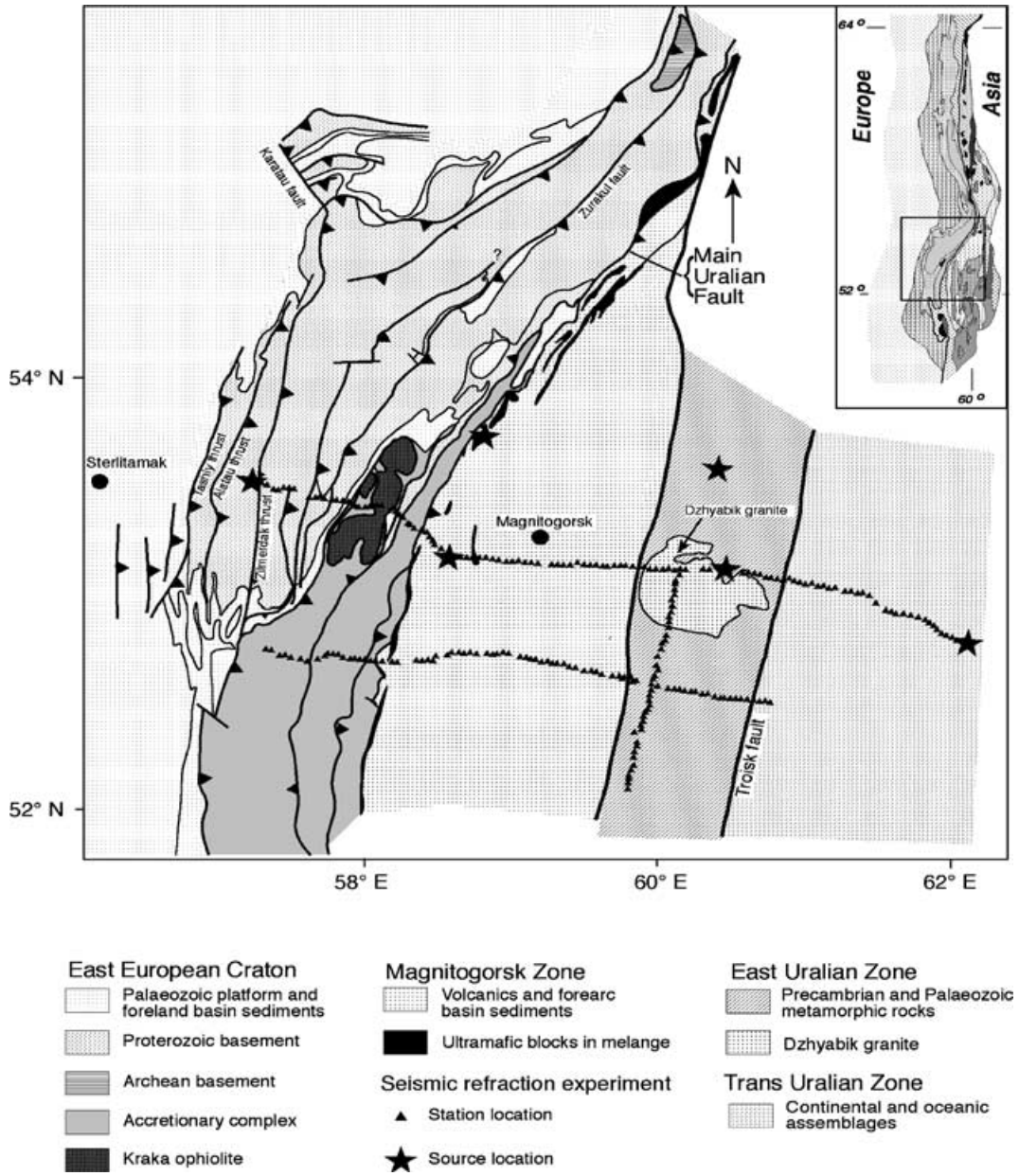

Figure 1. Location of the URSEIS'95 deep seismic experiment. Geologic sketch map indicating the major geologic units and tectonic structures of the southern Urals. Top inset map shows the location of the study area in the southern Urals. The inverted triangles indicate the receiver station location and the stars mark the shot points.

The acquisition of the fan recordings was designed so that the *PmP* reflection points would lie just beneath the main E–W profile along the CDP normal incidence data (Fig. 1) (Carbonell *et al.* 1996). The fan shots and receivers where located at approximately 55 km north and south of the main transect respectively. After processing the fan recordings were overlain on the wide-angle inline recordings so that the Moho events could be identified from the inline to the fan sections.

Table 1. Estimates for normal incidence two way traveltime for the Moho T_0 for the vertical and horizontal component wide-angle seismic data and, crustal average *P* and *S*-wave velocities used to calculate the hyperbolic time shift using eq. (1). These parameters have been computed as ray path averages through the velocity models determined by Carbonell *et al.* (2000).

	T_0 (s)	Shot 1 (km s^{-1})	Shot 2 (km s^{-1})	Shot 3 (km s^{-1})	Shot 4 (km s^{-1})
P-Wave velocity	15.0	6.45	6.60	6.60	6.50
S-Wave velocity —EW	26.0	3.72	3.81	3.81	3.75
S-Wave velocity —NS	26.0	3.72	3.81	3.81	3.78

3.2 Data description

The filtered, trace balanced and time corrected (shifted using eq. 1) wide-angle shot records display a prominent phase centred at approximately 15 s. This high amplitude arrival corresponds to the *PmP* reflection from the Moho. Fig. 2 illustrates that the Moho is controlled all along the cross-section by the different shot gathers. Shot 1 shows the *PmP* from the west, CDP 50, up to CDP 600. Shot 2 constrains the Moho between CDP's 650–1150. The Moho in this shot record is imaged as a high amplitude event dipping to the

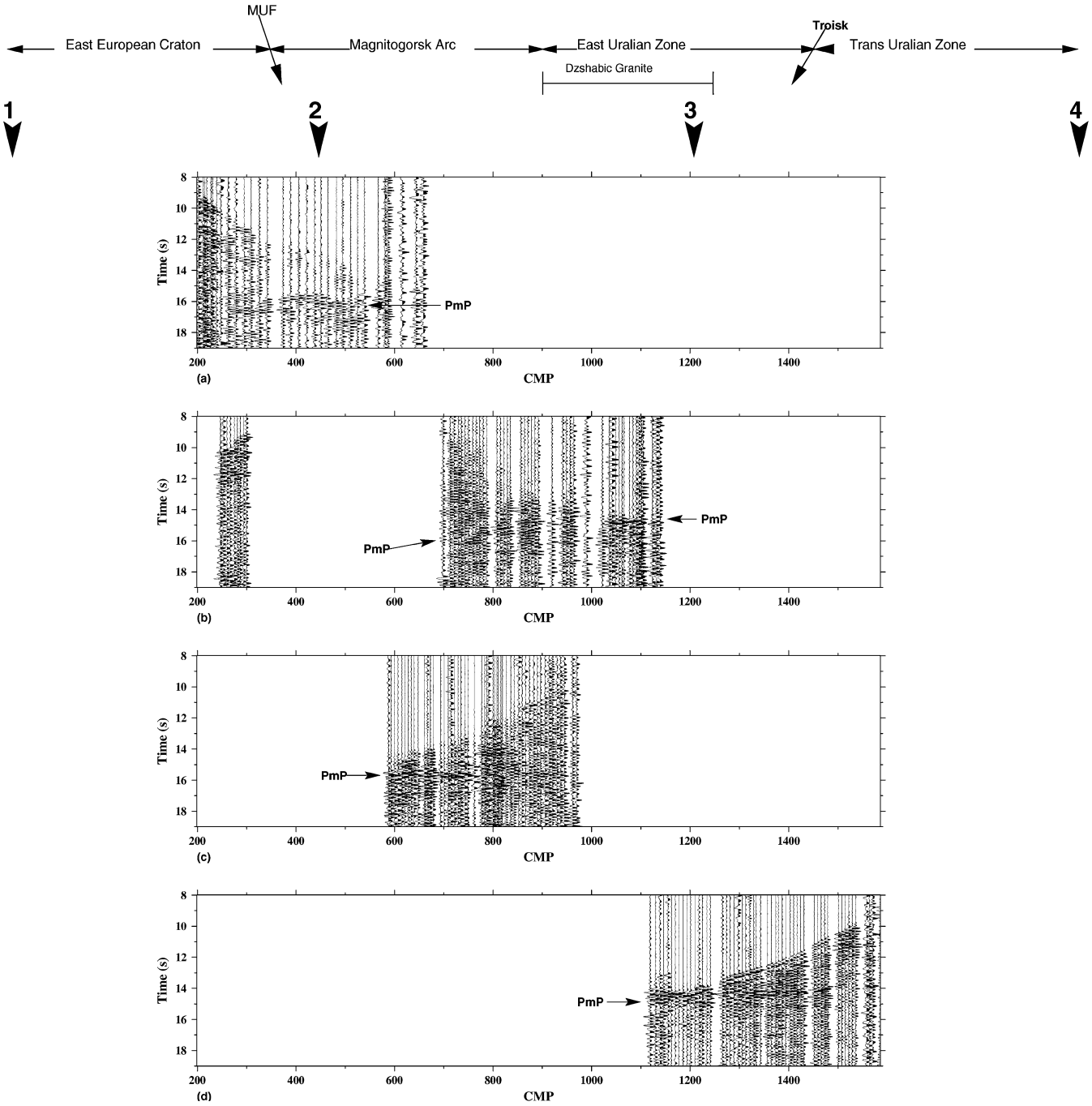

Figure 2. Wide-angle inline shots recorded along the URSEIS'95 seismic profile. (a), (b), (c), (d), correspond to shots 1, 2, 3, and 4, respectively. The shot gathers have been time shifted using eq. (1) (see text for explanation). Eq. (1) is based on a flat Moho. The time axis corresponds to two-way-travel times in (s) at half distance reflection points. *PmP* marks the Moho reflection. The shot gathers have been low pass filtered up to 6 Hz, following Carbonell *et al.* (2000).

west between 14–16 s. This shot constraints the eastern part of the root zone. Shot gather 3 images a high amplitude horizontal event located at 15.5 s and CDP's 575–975 this events places constraints on the depth of the root zone. The *PmP* in shot 4 is a high amplitude horizontal event located at 14.5 s, between CDP's 1110–1500.

The fan shot gathers do not display such a prominent *PmP* arrival. Nevertheless, once the fan sections and the inline shot records are overlain a relative high amplitude wave packet nearly coincides with the *PmP* interpreted from the inline wide-angle data (Fig. 3). See for example the relative high amplitude arrivals between 14–16 s between CDP's 1100–1200, and at 15 s between CDP's 400–500. Some prominent features are the amplitude differences between the inline wide-angle and the fan recordings. This amplitude difference is most probably due to offset. True amplitude plots of the *PmP* amplitudes as a function of offset indicate that the critical distance for the Moho is in the offset range of approximately 150–160 km. The fan records were acquired between 105–120 km offset, Fig. 4 indicates that the latter distances are still in the precritical range for the Moho. The fan records image arcuate events at lower crustal levels, for example between 12–16 s and CDP's 400–600 (Fig. 3).

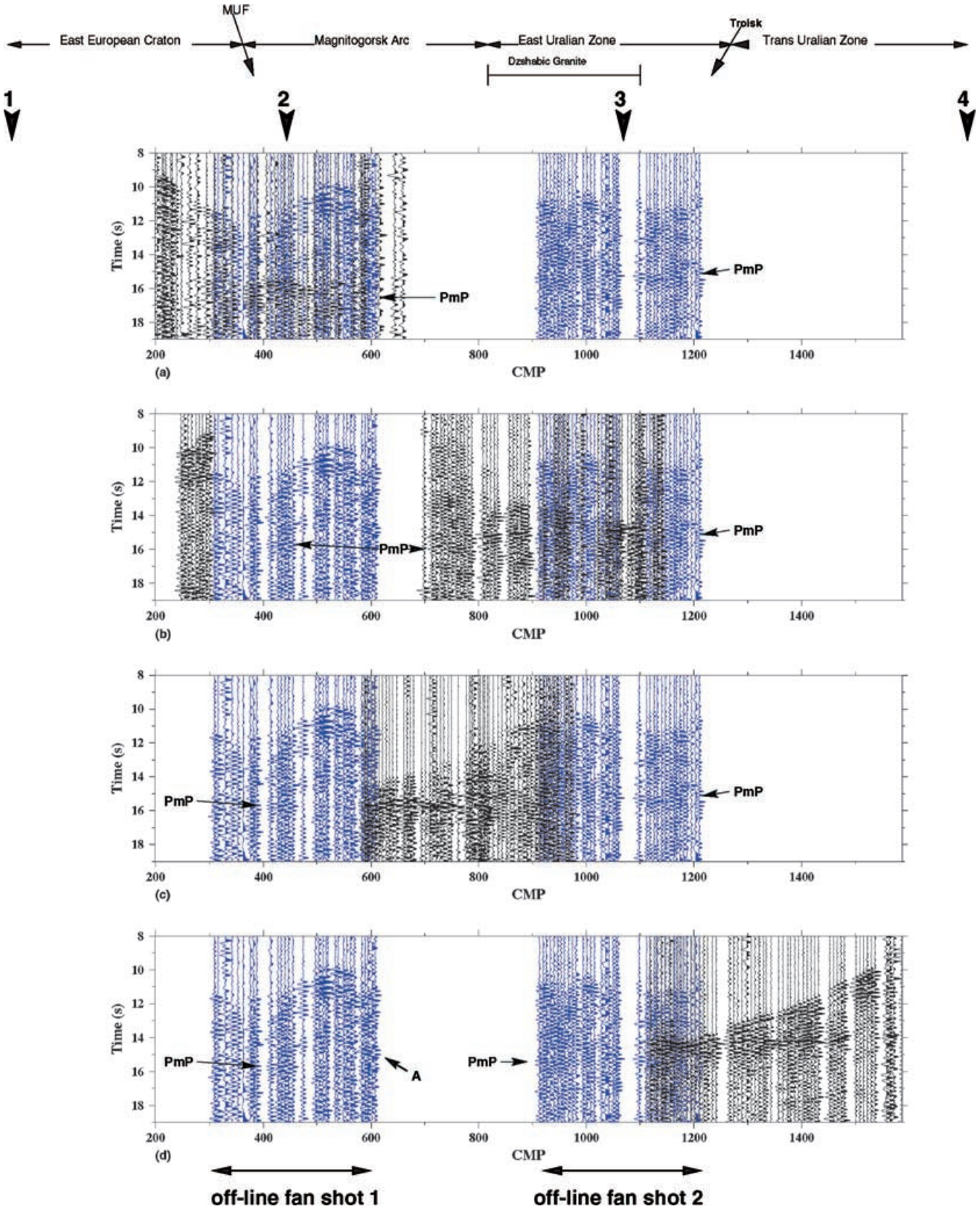

Figure 3. The same as Fig. 2, the wide-angle shot gathers 1, 2, 3 and 4 (in black) to which the fan recording have been overlayed (in blue). This illustrates the amplitude differences of the *PmP* phase between the wide-angle and the fan recordings. The arcuate reflection is also indicated (A). The lack of a high reflection coefficient at the sediment basement interface rules out this event as being a multiple of the first arrivals.

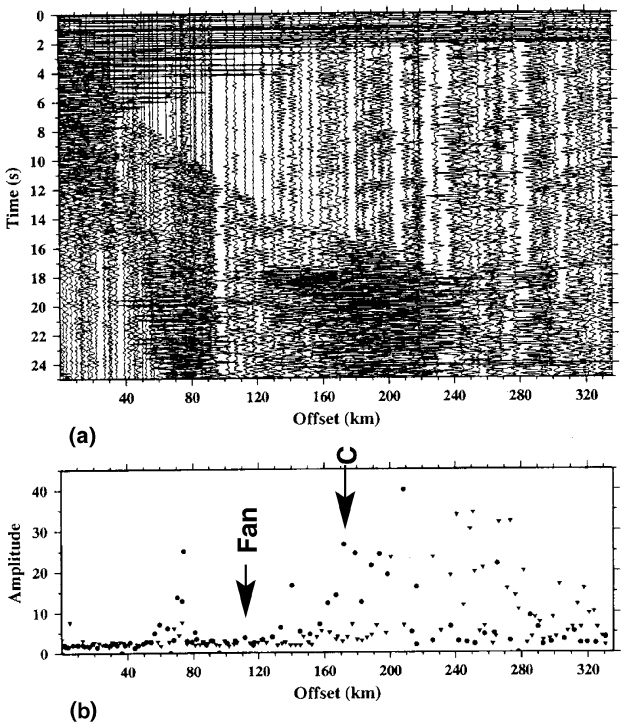

Figure 4. Amplitude behaviour of the *PmP* with offset (absolute value). (a) Trace balanced plot of Shot 1. The traces have been balanced by the RMS of the amplitudes within the window around the *PmP* phase (14–16 s). Traces have been time shifted using eq. (1). The time axis correspond to two-way travel times at half distance reflection points. (b) Graph of the maximum amplitudes within the 14–16 s window (around the *PmP*) for shot record 1 (solid circles) and shot record 4 (inverted triangles). Note the increase in the amplitude of the *PmP* beyond 150 km. **C** marks the critical distance. **Fan** indicates the offset at which the fan recording where acquired (pre-critical). The high amplitudes located at approximately 60 km offset correspond to *S*-wave energy.

Without a well developed low velocity sedimentary cover (Fig. 1), the amplitudes of this event are too high for it to be interpreted as a multiple of the first arrivals. This suggests a complex, probably boudin-like structure within the lower crust. This is further supported beneath the root zone by arcuate events (D) identified in the wide-angle stacks (Fig. 5).

One of the most peculiar observations of the normal incidence Vibroseis and explosive data sets (Echtler *et al.* 1996; Knapp *et al.* 1996; Steer *et al.* 1998a) is the lack of a well defined Moho beneath the root zone. These data sets imaged a high amplitude *PmP* beneath the EEC and beneath the Siberian terranes west and east of the root zone, respectively. The best resolved images of the Moho beneath the root zone are provided by stacking the inline wide-angle shot records (Fig. 5). The vertical and horizontal component wide-angle stacked sections image a high amplitude *PmP* beneath the root zone and high amplitude east dipping sub-Moho events (Fig. 5) for example in CDP 800 at 19 s in the vertical component and at 34–35 s in the horizontal components. The horizontal components are characterized by a frequency content similar to the frequency content of the vertical components. Because the *S*-wave velocities are lower than the *P*-wave velocities, *S*-waves have higher resolution than *P*-waves. The east dipping upper-mantle events (D) are imaged by the horizontal component wide-angle stacks (Fig. 5).

The *PmP* phase can be imaged, approximately, from 75 to 220 km in shot record 1 and from 75 to 340 km in shot record 4 (Fig. 6). The *PmP* is followed by a coda approximately 2 s wide. Additionally, both records display between 250–340 km offset, a phase which can be interpreted as a *Pn* phase, however we prefer to label it P^*n. Synthetic modelling studies by several authors (Ryberg *et al.* 1995; Tittgemeyer *et al.* 1996; Enderle *et al.* 1997) have revealed that the high frequency *Pn* featuring relatively high apparent velocities (above 8 km s^{-1}) observed in wide-angle shot records can be interpreted as a phase travelling through a laterally heterogeneous layer within the upper mantle. The P^*n phase identified in Fig. 6 is characterized by relatively high frequencies (frequencies above 8 Hz) and by apparent velocities which range between 7.5 to 8.5 km s^{-1}. The limited offset range where this phase can be identified prevents a good velocity resolution. Therefore, we interpret P^*n as a phase similar to *Pn* but travelling within the crust–mantle transition zone.

4 SYNTHETIC SEISMIC MODELLING

4.1 Methodology

The wide-angle stacks and the fan sections reveal the large scale structure of the lower crust and show the geometry of the Moho. To estimate the detailed internal architecture of the Moho, the dynamic characteristics of the *PmP* and P^*n phases were analysed and modelled. The forward modelling was done using 1- and 2-D seismic wave propagation algorithms. Additionally, the modelling had to address the effects of low velocity surface cover on the seismic signature of the deep structures to estimate the influence of the Silurian and Devonian volcaniclastics and other sediments mapped in this area. The resulting models need to account for the features observed in the recorded normal incidence and wide-angle data sets.

The normal incidence CDP stacked sections revealed a high amplitude Moho reflection beneath the EEC and beneath Siberian terranes to the east. For approximately 200 km beneath the central part of the profile, the image lacks a Moho reflection. Steer *et al.* (1998a) interpreted this as evidence for a transitional Moho. The wide-angle reflection data reveals a broad and well developed *PmP* reflection beneath this zone (Carbonell *et al.* 1998) suggesting a complex heterogeneous crust–mantle transition towards the centre. In order to address this apparent contradiction we calculated the synthetic seismic signature of idealized crust–mantle transition models: a gradient zone, a layered structure, a step discontinuity with topographic relief and, a laterally heterogeneous layer. For each of these classes of models, several iterations of the modelling algorithms were required to estimate the geometrical parameters that characterize each model so that it would simulate more closely the observed data; for example, the thickness of the crust–mantle transition, the scale of the lateral heterogeneities, the scale of the topographic relief, etc. A final set of model studies included the effect of low velocity surface layers, which is not commonly addressed in seismic interpretations. This last set of models revealed that the size of the impedance contrast at the sediment–basement interface is of critical importance for the waveform and coda of deep reflectors.

A reflectivity modelling algorithm (Fuchs & Müller 1971; Kennett 1983) was used to generate 1-D velocity models (laterally homogeneous models) and investigate the seismic signature of gradient zones, and layered sequences, with and without a shallow surface sedimentary layer. A 2-D explicit, elastic finite difference modelling code (Sochackic *et al.* 1991) was used to simulate the seismic signature of laterally heterogeneous structures such as boudins and layers with irregular topography. Synthetic seismograms were

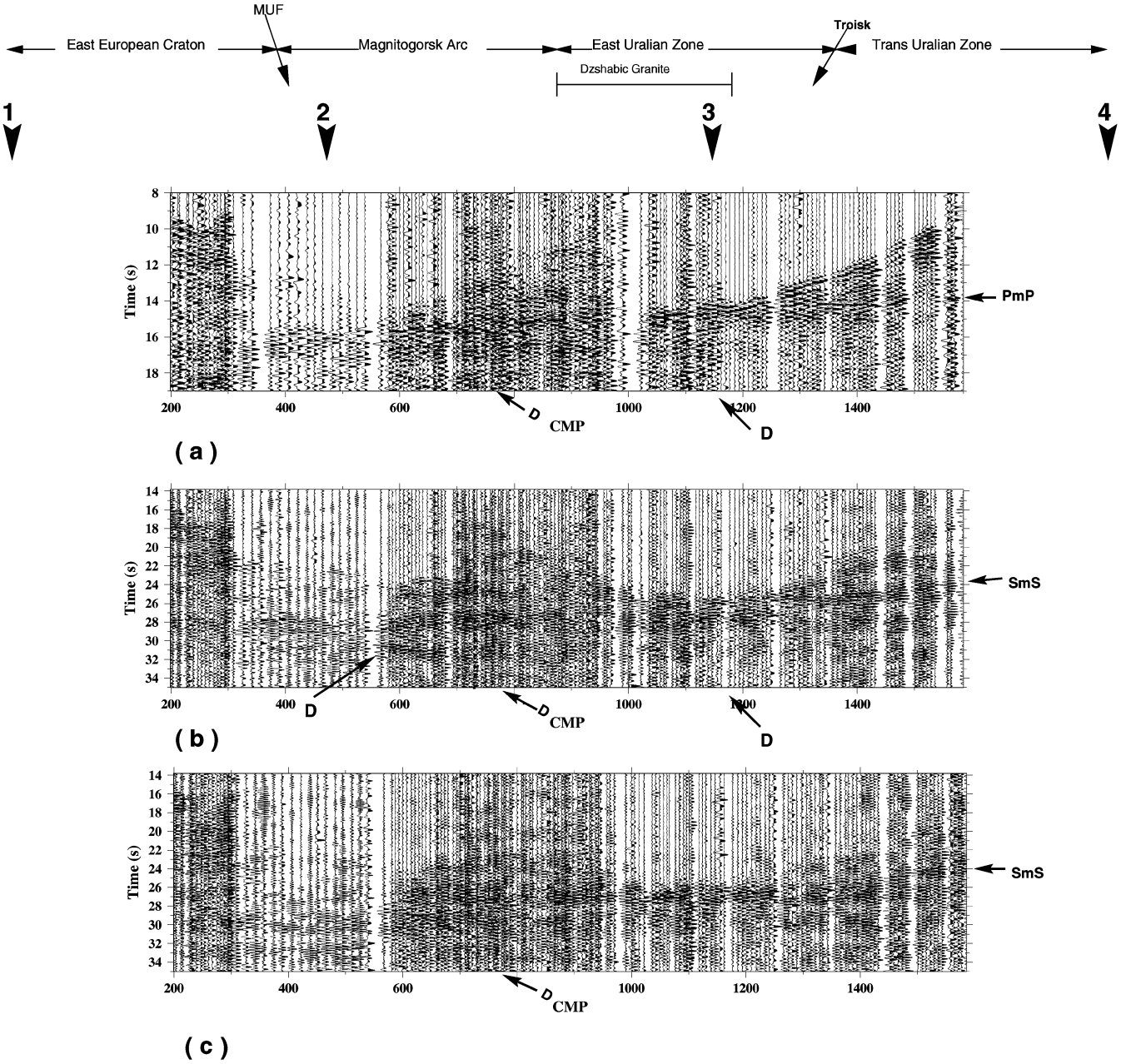

Figure 5. Stacked images of the wide-angle inline recordings. (a) Stack of the vertical components record sections. (b) and (c) are the stacks of the NS and EW horizontal components of the wide-angle records. *PmP* marks the *P*-wave reflected from the Moho. *SmS* the *S*-wave reflected from the Moho, and D dipping mantle events. A sketch of the geology showing the different domains, and the position of the main fault zones is overlayed on top of the figure. MUF and Troisk mark the Main Uralian and Troisk fault zones. The numbered arrows indicate the surface location of the shot points.

calculated for these models with and without a low velocity surface layer.

4.2 Parameters

The lower crust in the root zone is mostly constrained by the observed wide-angle stacks and the fan recordings. In order to constrain the detailed structure of the crust–mantle transition, the characteristic features of the shot records that we want to simulate are:

(i) Lack of or very weak high amplitude *PmP* at normal incidence. The Vibroseis and explosion CDP do not image the Moho beneath the root zone.

(ii) The amplitude behaviour with offset of the *PmP* phase. A high amplitude peak is observed at approximately 150 to 160 km offset. This is interpreted as critical distance.

(iii) A 1–2 s long *PmP* coda. The *PmP* wavelet is rich in reverberations between 100 to 200 km offset.

(iv) A relatively high frequency P^*n phase visible as first arrival at approximately 225 km offset in shot records 1 and 4.

These features are sufficient to differentiate between models belonging to three different classes:

(i) Gradient models representing a smooth geological transition from crust to mantle.

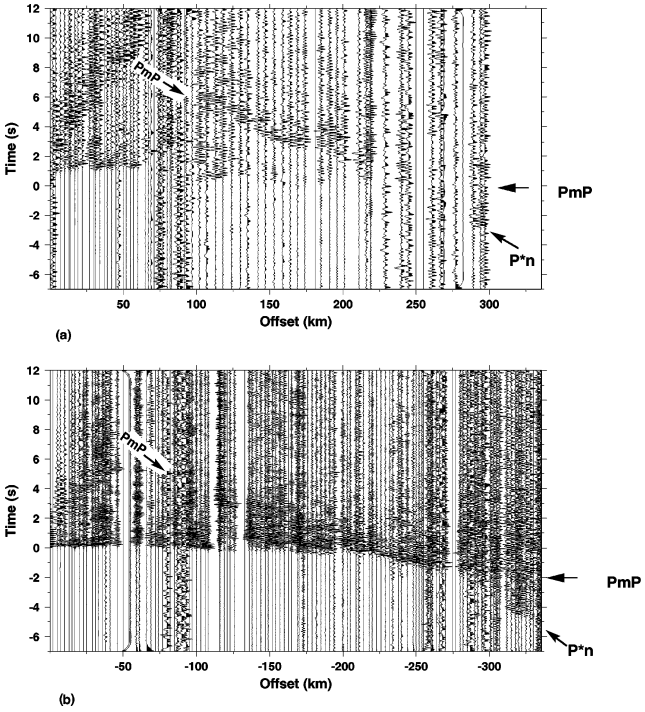

Figure 6. Wide-angle shot gathers for shot 1 (a) and 4 (b) reduced for a velocity of 6.0 km s^{-1}. *PmP* and P^*n phases are also indicated. In order to be able to compare both shots, shot 4 has been flipped so that left corresponds to east and right to west. *PmP* can be observed from approximately 100 km to 350 km. P^*n can be identified beyond 250 and is characterized by relatively high frequencies. Note that P^*n is interpreted as a phase similar to *Pn* but travelling within the heterogeneous crust–mantle transition while *Pn* travels within a laterally heterogeneous layer within the upper mantle.

(ii) A crust–mantle transition with alternating high and low velocity layers.

(iii) A crust–mantle transition with laterally variable physical properties. The lateral variability can be achieved in two different ways:

(a) The Moho can be considered as a rough surface with topographic relief.
(b) The crust–mantle transition can consists of laterally discontinuous layering (boudin-like structures).

The average crustal velocity is constrained by conventional interpretation of the wide-angle reflection/refraction (Carbonell *et al.* 2000). Reasonable values for the physical properties (Vp, Vs, ρ) for the Moho depth range were obtained from laboratory measurements of possible lower crustal rocks (Kumazawa *et al.* 1971; Kern & Richter 1981; Fountain *et al.* 1994; Christensen & Mooney 1995; Rudnick & Fountain 1995). To simulate the explosive source rich in low frequencies used in the URSEIS'95 experiment a minimum phase wavelet with a frequency content between 3 and 25 Hz was used as the source signal. All the synthetic seismic data are plotted with a velocity reduction of 6 km s^{-1}, while in the stack images the time axis corresponds to two way traveltimes.

4.3 Gradient Moho models

A transitional zone can be modelled as a layer characterized by a gradual increase in velocity (gradient) from crustal to mantle values. The sharpness of the velocity change is dependent on the thickness

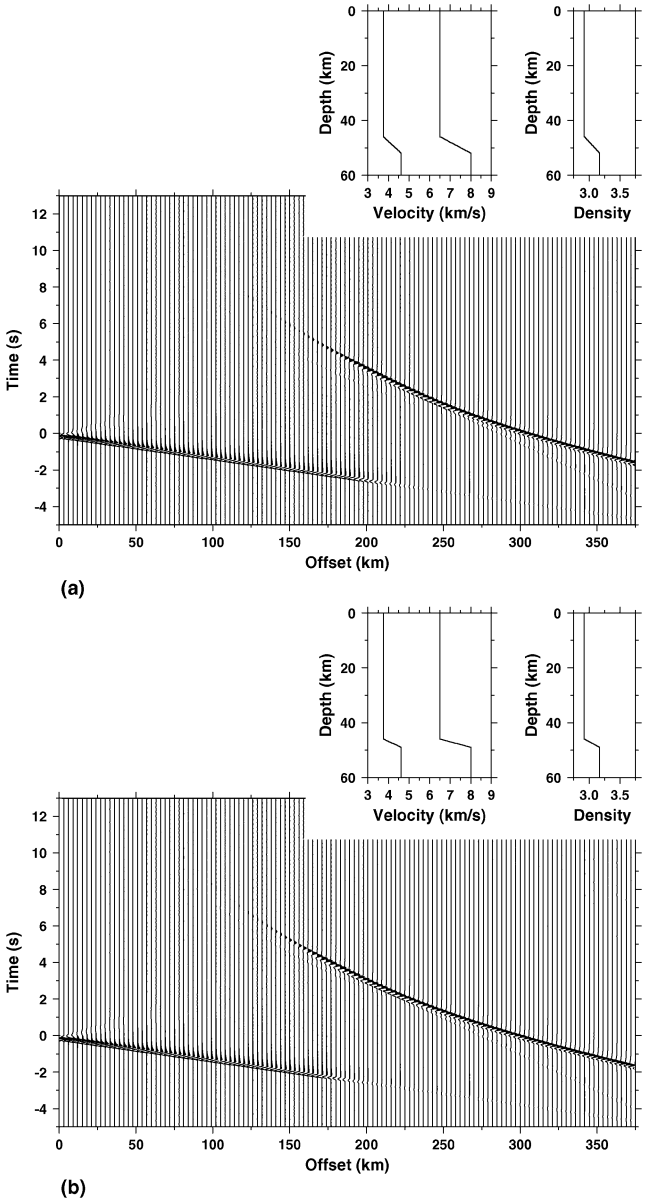

Figure 7. Velocity profiles for transitional models for the Moho beneath the root zone and the seismic response calculated using a reflectivity algorithm (Fuchs & Müller 1971). In both models, the physical properties increase from average crustal values to values characteristic of the mantle. The only feature that changes is the thickness of the Moho transition. The overall thickness if the Moho transition is 6 km thick in model (a) and 3 km thick in model (b). Notice the lack of P^*n at far offsets, which depends on the velocity gradient in the upper mantle. The times have been reduced for a velocity of 6 km s^{-1}.

of the Moho (gradient zone). The synthetic seismograms obtained with the reflectivity algorithm (Fig. 7) for a gradient layer indicate that at normal incidence a gradient zone does not generate a visible reflection, the amplitude of the *PmP* increases with offset. The *PmP* is characterized by a short wavelet lacking a visible coda. The synthetic seismograms estimated for a gradient zone feature a weak low frequency P^*n phase which is not comparable with the $P * n$ observed in the field data. The amplitude of the P^*n arrival can be increased by introducing a small gradient beneath the Moho discontinuity, however, such a model cannot reproduce the frequency characteristics of the observed data.

4.4 Layered Moho models

Layered models produce prominent *PmP* signals, and a visible P^*n (Fig. 8). These layered models are characterized by two parameters, thickness of the Moho transition (H) and thickness of the internal layers (h). We explored the parameter space computing synthetic seismograms for models with different values for H and different values for h. The modelling suggests that the duration of the *PmP* coda is controlled by the thickness of the transition layer (H). The number of wiggles in the phase is controlled by the thickness of the internal layering. For example, two transition models with the same internal layering h ($h = 600$ m), one characterized by $H = 3$ km and a second featuring a $H = 6$ km, the thicker transition produces the longer *PmP* phase (compare Figs 8a and c). On the other hand two models with the same $H = 6$ km, one featuring $h = 25$ m and a second with $h = 600$ m, the latter produces a *PmP* characterized by a reverberatory pattern (more wiggles, compare Figs 8a and b). For thin internal layers (h smaller than $1/4\lambda$ wavelength) the precritical *PmP* features two amplitude maxima (Fig. 8b) while for larger h (600 m) the *PmP* features a reverberatory pattern (Fig. 8a). All the layered models do not require a velocity gradient in the upper mantle to produce a visible P^*n phase which can be identified at approximately, 250 km offset. Similar models are further discussed by Tittgemeyer *et al.* (1996) and Enderle *et al.* (1997).

4.5 The effects of low velocity surface layer

Theoretical calculations (Kanasewich *et al.* 1983; Holliger & Robertsson 1998) and high resolution seismics have shown that the shallow subsurface is were most of the energy conversions take place and where the seismic velocities present the largest variations, therefore, this is the structure that interferes the most with the deep seismic wavefield. In order to investigate how shallow low velocities can affect the deep seismic events, the 1-D models were modified by adding a 2 km thick low velocity layer at the surface. The velocity of this layer has been decreased from 6.0 km s^{-1} to 4.0 km s^{-1} in successive iterations of the reflectivity modelling. This implies an increase in the reflection coefficient from 0.1 to 0.25 at the basement interface. The presence of the low velocity layer causes peg-leg multiples which can be identified paralleling the first arrival up to 110–125 km offsets (Fig. 9). As it is evident from Fig. 9, the existence of this layer also affects the *PmP* phase. The length of the *PmP* coda is increased by the addition of peg-leg multiples of the *PmP* generated at the shallow subsurface. The peg-leg multiples generated by the shallow low velocity layer introduces reverberations in the *PmP* phase. The amplitudes of these reverberations depend on the magnitude of the reflection coefficient of the basement interface (compare Figs 9a and b).

4.6 Laterally heterogeneous Moho models

Heterogeneous Moho models in which the velocity varies laterally can be achieved in two different ways: a velocity step with topographic relief (Larkin *et al.* 1997), or by laterally discontinuous layering. Synthetic seismograms for four sets of models have been obtained which include: step discontinuity with topographic relief with and without a low velocity surface layer, and a Moho model consisting of laterally discontinuous layers with and without a low velocity cover. The elastic finite difference seismic simulations reveal that the effects of a shallow low velocity layer for these laterally heterogeneous models are very similar to the ones observed in the reflectivity simulations. The most significant differences on the

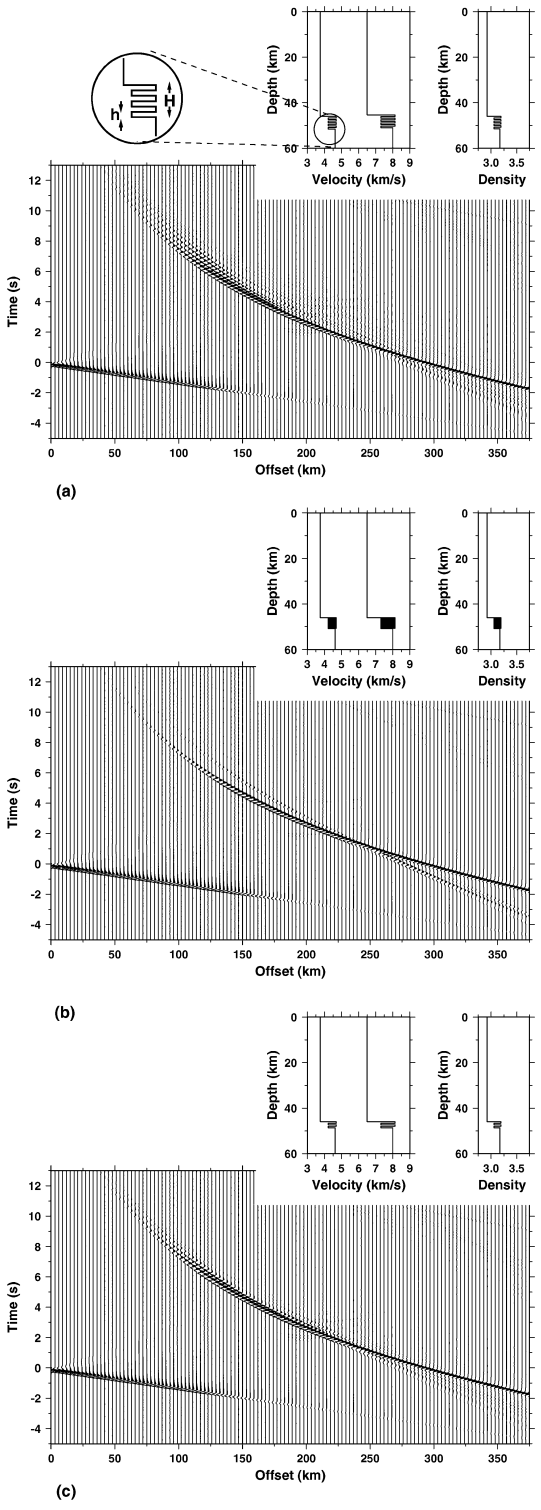

Figure 8. Velocity profiles for layered crust–mantle transition models and their seismic response calculated using a reflectivity algorithm (Fuchs & Müller 1971; Kennett 1983). The Moho consists of a packet of layers of alternating high and low velocities (bimodal velocity distribution). These models feature different thickness of the Moho transition (H) and different thickness of the internal layering (h). (a) The layered model is characterized by a H of 6 km and a h of 100 m. (b) The layered model is characterized by an H of 6 km and an h of 600 m. (c) The layered model is characterized by an H of 3 km and an h of 600 m. Note the differences in the seismic response between the three models, specially in the width of the coda between 75–175 km and the Pn. The times have been reduced for a velocity of 6 km s^{-1}.

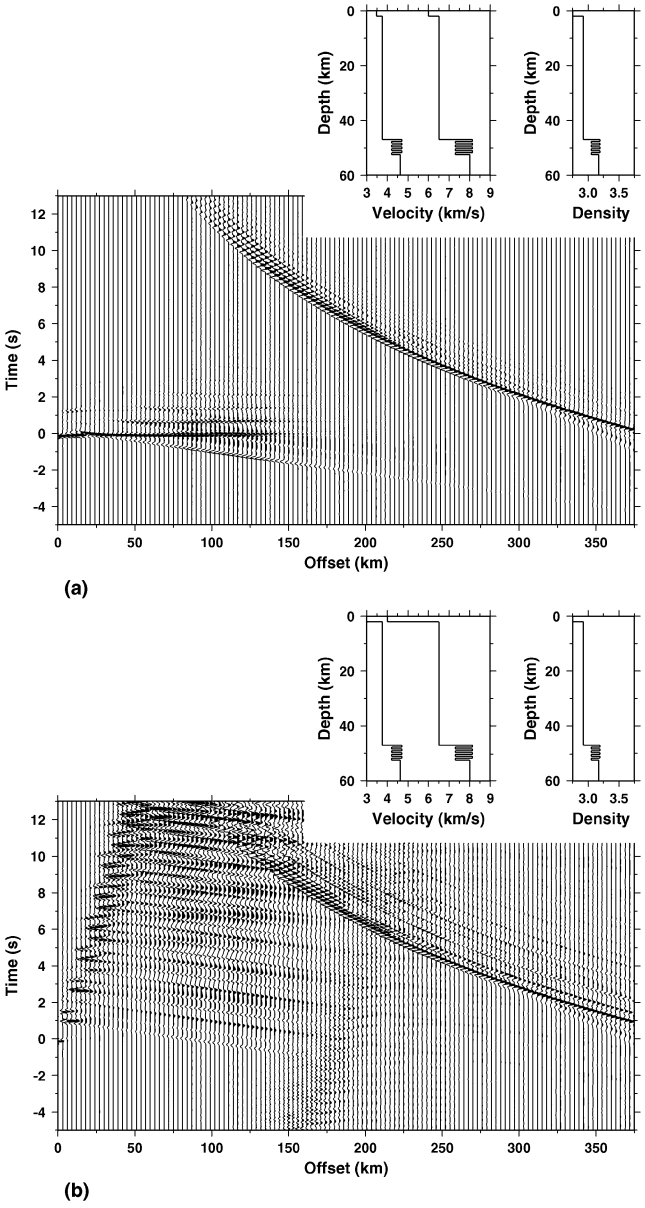

Figure 9. Synthetic seismic response for velocity profiles for layered Moho models illustrating the effect of a shallow low velocity layer the synthetic seismograms have been calculated using the reflectivity algorithm (Fuchs & Müller 1971). In (a) the *P*-wave velocity of the shallow layer is of 6.0 km s^{-1}. In (b) the *P*-wave velocity of the shallow layer is of 4.0 km s^{-1}. This illustrates the influence of the reflection coefficient of the basement interface in the seismic wavefield. Note the increase of the *PmP* coda in (b). This illustrates the need for a high reflection coefficient for the basement interface which is probably not the case in this area. The times have been reduced for a velocity of 6 km s^{-1}.

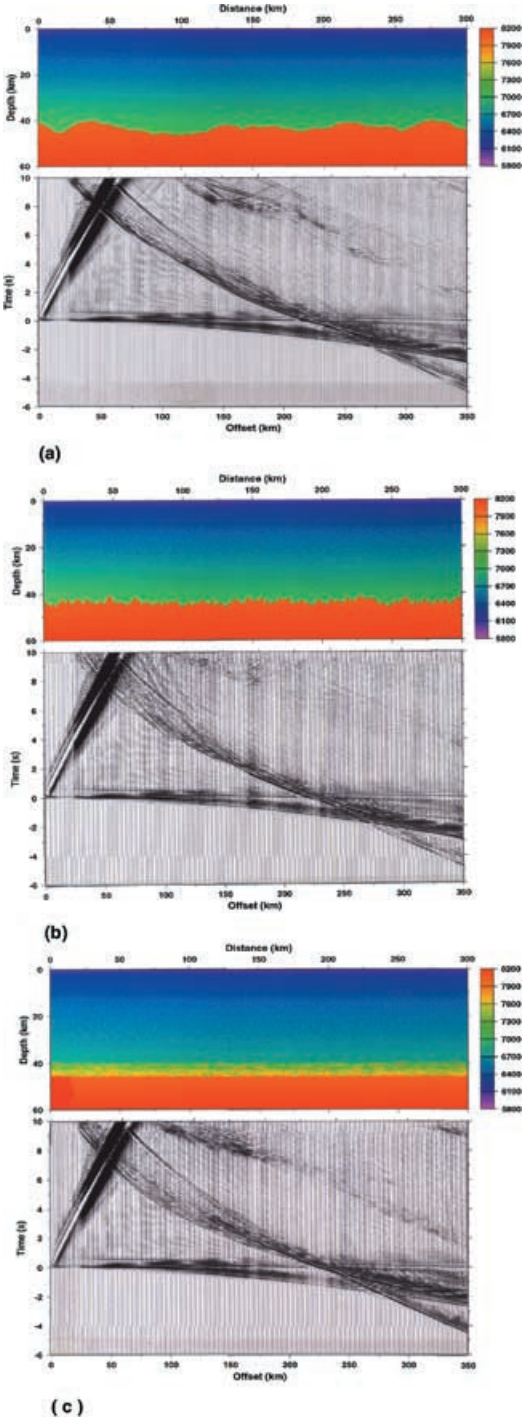

Figure 10. 2-D velocity models for a laterally heterogeneous Moho transition and their seismic response calculated using a finite difference elastic wave propagation algorithm (Sochackic *et al.* 1991). (a) Laterally heterogeneous Moho, heterogeneity is achieved by an irregular topography for the Moho. The difference between the maximum and the minimum of the Moho topography can be considered as the thickness of the Moho transition. The lateral correlation length is 20000 m. (b) is the same as (a) but with a lateral correlation length of 5000 m. (c) Laterally heterogeneous 6 km thick transition zone, the heterogeneities are ellipsoids distributed at random, with dimensions: vertical axis between 400–800 m; horizontal axis between 600–2000 m. Note that the dominant frequency of the wide angle seismic data is below 6 Hz, which suggests a vertical resolution of approximately 600 m (see text for an explanation). The times have been reduced for a velocity of 6 km s^{-1}.

seismic signatures are the ones due to the geometry of the crust–mantle transition. Geological mapping of the surface structures and the Vibroseis and explosive CDP data suggest relatively low velocities (of approximately 5.5–5.8 km s^{-1}) for the upper 1–2 km which rapidly increase to 6.2 km s^{-1}. These layers vary laterally in nature and composition, therefore we have considered that a velocity gradient form 5.8 to 7.1 km s^{-1} was a physically reasonable average crustal velocity function for the 2-D finite difference synthetics. Three examples are shown in Fig. 10, these examples feature a crust characterized by a gradient velocity form 5.8 to 7.1 km s^{-1}. As can

be seen in Fig. 10, both classes of model generate a wavefield which is the result of the interference of the back scattered energy consisting mostly of diffractions. At normal incidence, they don't display prominent reflections, however, at far offsets, the constructive interference of the diffraction tails generate laterally more extensive events (Levander & Holliger 1992). The synthetic shot records generated by these laterally variable velocity models are the ones that most closely resemble the wide-angle shot gathers acquired by the URSEIS-95 (Fig. 10).

4.6.1 Step discontinuity with topographic relief

The parameters used to characterize this Moho structure are: its thickness and the degree of roughness of the interface. The thickness of the transition is determined by the difference between the maximum and minimum of the topography (6 km). The degree of roughness is represented by the correlation length of the topographic profile. The topographic profiles were generated following Goff & Jordan (1988). Qualitatively, these models display high amplitude arcuate diffractions which generate a *PmP* phase with a high amplitude and long coda, and a well defined critical distance which is located at approximately 150–170 km and that it is best defined in the models with longer correlation length (smoother topography). All models display a P^*n phase (Fig. 10). At normal incidence these models feature weak reflectivity.

4.6.2 Laterally discontinuous layering

A Moho structure consisting of laterally discontinuous layering has been modelled as a 6 km thick boudinage structure were the boudins where characterized by variable velocities within the range 7.2–7.8 km s^{-1}. These boudins are embedded in a layer that features a gradient velocity function (from 7.2 to 8.0 km s^{-1}). This structure generates a seismic signature which is the interference of the diffractions with travel times before the *PmP* and velocities $<$7.9 km s^{-1} in the layering (Fig. 10) caused by the individual boudins. A 1–2 s long *PmP* and a P^*n are generated by this heterogeneous structure. The *Pn* would be generated below this transition zone.

5 DISCUSSION AND IMPLICATIONS

5.1 Stack images

The lack of a distinct Moho reflection and the existence of clouds of scattered energy within the root zone in the normal incidence reflection sections (Knapp *et al.* 1996; Steer *et al.* 1998a) favours a strongly heterogeneous lower crust–mantle transition zone beneath the Magnitogorsk volcanic arc. Arcuate reflections, diffractions located in the root zone imaged by the vertical and horizontal wide-angle stacks, specially in the more resolutive *S*-wave images, reveal either the existence of relics of an east dipping slab or they can be interpreted as arcuate diffractions generated by a highly heterogeneous boudinage structure (Fig. 5).

5.2 1-D seismic modelling

CDP sections of many cratonic regions are characterized by a non-reflective Moho (Brown 1991). Traditionally, to reduce precritical energy in synthetic seismograms, seismologists introduce a layer with velocities increasing linearly form values typical for the lower crust to values characteristic of the upper mantle. Therefore, the lack of reflectivity at normal incidence and the increase in reflected amplitudes of the *PmP* with offset can be explained by gradient velocity models (Fig. 7). However, these gradient velocity models do not generate a P^*n phase. The P^*n arrival interpreted in Shot records 1 and 4 (Fig. 6) constitute evidence for a complex velocity structure for the crust–mantle transition.

The *PmP* is better imaged after low pass filtering the data up to 4 or 6 Hz (Carbonell *et al.* 2000). The commonly used -$\lambda/4$- criteria to estimate the vertical resolution reveals for these low frequencies and an average velocity of 7.2 km s^{-1} an approximate thickness for the internal layering of the crust–mantle transition (h) of 600 m. Seismic modelling using a reflectivity algorithm (Fuchs & Müller 1971) of a transition consisting of packets of layers of different thickness suggests that relatively thick layers are required to produce the observed coda with the low frequencies that characterized the *PmP* arrival in the shot records. Fig. 8 illustrates the differences in the reverberation pattern of the coda between three models (a: $H = 6$ and $h = 100$, b: $H = 6$ and $h = 600$ and, c: $H = 3$ and $h = 600$). All three models generate an identifiable P^*n phase. However, the pattern of the *PmP* coda changes from model to model. The coda of Model a, (a thinly layered transition zone) images the top and bottom of the transition structure. The *PmP* and P^*n phases that are generated by Model b simulate more closely the observed seismic signature. An approximately 1 s long reverberation (coda) is generated by this model between 50 and 175 km offset, and a P^*n phase is also visible beyond 225 km (Fig. 8). The *PmP* coda generated by Model c which is characterized by a thin transition layer ($H = 3$) does not last long enough to be comparable to the observed in shot 1 between 100–200 km for example. Therefore, this 1-D reflectivity seismic modelling of the wide-angle seismic data favours an approximately 6 km thick crust–mantle transition consisting of relatively thick layers (600 m).

Layered structures such as the one favoured by the wide-angle data can cause normal incidence reflections and therefore this does not agree with the explosive and Vibroseis CDP data sets. These data sets do not image the Moho beneath the root zone. There are two reasons that could possibly account for the lack of Moho reflections in the CDP sections (Knapp *et al.* 1996; Steer *et al.* 1998a,b):

(i) A crust–mantle transition consisting of layers of $h = 600$ m requires frequencies lower than 6 Hz for constructive interference (using the -$\lambda/4$- criteria) to enhance the normal incidence reflections. These low frequencies were not recorded by the normal incidence (Vibroseis and explosive) seismic reflection CDP data (Knapp *et al.* 1996; Steer *et al.* 1998a,b) because the natural frequency of the geophones used for this acquisition was of 10 Hz. Nevertheless, for the wide-angle experiment, geophones with a natural frequency of 4 Hz were used, and a low frequency *PmP* phase was identified in the shot gathers (Carbonell *et al.* 1996, 2000).

(ii) Lack of penetration or localized attenuation (Q^{-1}) could prevent the source signal from reaching the Moho.

Simple layered models that closely simulated the dynamic characteristics of the *PmP* and P^*n wide-angle phases consisted of layered sequences of alternating high and low velocities. The acoustic impedance contrast in the layered transition zone of Fig. 9 is close to 0.08. Acoustic impedance values of 0.06–0.1 have been claimed to explain the reflectivity of the lower crust (Hale & Thompson 1982; Deemer & Hurich 1994). Therefore, this impedance contrast is enough to produce visible reflections without the need for constructive interference. Then the lack of a Moho reflection at normal incidence is probably not a result of the high pass filter effect due to the natural frequency of the geophones. The explosive source

seismic reflection transect was able to image upper-mantle features such as the Alexandrovka and Nikolaevka reflections sequences (Steer *et al.* 1998a,b). Therefore, attenuation and/or lack of penetration can not be claimed for the entire transect only in the root zone. Nevertheless, a cloud of backscattered energy is imaged by the explosion CDP stack in the root zone. Steer *et al.* (1998a) interpreted east dipping reflection fabrics beneath the root zone as resulting from a relic of subducted crust. These are evidences against high Q^{-1} values in this area.

PmP coda can also be a result of high reflection coefficients at the near surface structures. This reflectivity causes duplications of the Moho arrival masking its internal structure and suggesting a layered zone. This coda is generated by near surface high amplitude reflection coefficients. In order to have high amplitude peg-leg multiples of the Moho reflection that would effectively contribute to the *PmP* coda, high impedance contrasts are required. Surface geology indicates that most of the URSEIS'95 profile is overlaid by Upper Silurian to Upper Devonian volcanics and volcaniclastics, and Carboniferous sediments which most probably contribute to the seismic signature of the Moho.

5.3 2-D seismic modelling

Laterally heterogeneous models constitute the third class of models considered. These models can account for all the observed features in the seismic wavefield. Laterally heterogeneous models can be achieved by assuming that the Moho is an irregular topographic discontinuity and by introducing laterally discontinuous layers (heterogeneities).

The reflection coefficients for an irregular topographic discontinuity at different angles of incidence have been calculated by Dainty & Schultz (1995). They demonstrate that as the roughness of the interface increases the normal incidence reflection coefficient decreases, and the critical and post-critical reflection coefficients increase. The elastic finite difference simulations of a Moho with high topographic relief illustrate the increase of the critically scattered energy. The increase in the amplitude of the *PmP* is a result of constructive interference of far offset diffractions generated by the roughness of the Moho discontinuity (Fig. 10). An irregular Moho does not produce a zone of high reflectivity at normal incidence (Larkin *et al.* 1997). The vertical-incidence weak events are mostly backscattered energy. This feature is similar to the seismic response of a gradient layer. A rough crust mantle boundary can explain the amplitude character of the *PmP*. Notice that a decrease in the roughness increases the reflectivity at pre-critical offsets (Fig. 10). The roughness of the Moho is also responsible of the coda which follows the *PmP* arrival. Roughness on the scale of a few km (5 km in model Fig. 10a) causes the amplitude response of the normal incidence and wide angle data. Finally, this class of models generates a visible P^*n from within the rugged surface.

An heterogeneous Moho model consisting of a laterally discontinuous layering (boudin like structures) adequately simulates the characteristic features of the seismic field at normal incidence and at wide-angles. The length and magnitude of the reflections are strongly dependent on the horizontal dimensions of the layering (horizontal scale of the boudins). A horizontal scale within the range of 600–1000 m reproduces a weak backscattered pre-critical wavefield, a high amplitude *PmP* between 75–175 km offset with an approximately 1 s long coda and, a visible P^*n at offsets beyond 225 km (Fig. 10c).

The interpreted P^*n is a phase comparable to the Pn but generated within the crust–mantle transition zone. Synthetic seismic modelling by Tittgemeyer *et al.* (1996) demonstrated that Pn can be produced by a randomly layered structure at the base of the crust. This heterogeneous layer acts as a waveguide (whispering gallery effect Menke & Richards 1983). The resulting P^*n is a multiply refracted, guided wave travelling within a laterally heterogeneous layer. The dynamic characteristics of the Pn have been thoroughly studied and modelled for the PNE data (Ryberg *et al.* 1995; Tittgemeyer *et al.* 1996; Enderle *et al.* 1997). The large offsets recording of the Peaceful Nuclear Explosions (PNE) (Egorkin & Mikhaltsev 1990) reveal a relatively high frequency *Pn*. Although, the URSEIS'95 wide-angle recording have very limited offset, the P^*n is also imaged as a high frequency phase.

5.4 A crust–mantle transition model

The *P* and *S* wide-angle stacks and the seismic modelling favour a model for the crust–mantle transition beneath the root with strong lateral and vertical variations. The heterogeneities inferred probably extend to the upper mantle (Fig. 11) in order to generate the observed P^*n phase. These strong laterally and vertically inhomogeneous Moho models account for all the observations: lack of normal incidence reflectivity, high amplitude *PmP* characterized by a 1–2 s long coda, and a visible high frequency P^*n phase. This strongly heterogeneous root zone is probably the result of the interference between the structures produced during the successive collisions and the later re-equilibration processes. Two alternative geological interpretations can generate such a structure (Fig. 11). (1) Magmatic underplating at the base of the crust due to partial melting and mixing of the subducted pieces of the crust from the EEC and the Siberian terranes, and (2) upward migration of and eclogite metamorphic front. These two end members have been used commonly to account for non-reflective crust–mantle transition (Nelson 1991; Jarchow *et al.* 1993; Baird *et al.* 1995). In the first model the magmatic bodies intruded in the deep crust are responsible for the vertical and lateral variations of the physical properties which account for the arcuate events and the characteristic features imaged by the wide-angle recordings. In the second model, all these seismic features are accounted for by the heterogeneities generated by different degrees of eclogitization and/or the internal structure of the eclogitized rocks within the root zone.

Steer *et al.* (1998a) interpret the lack of Moho reflectivity in the CDP sections as evidence that the Moho is a transition structure. The characteristic features of the seismic signature at normal incidence and wide-angle discussed above suggest that the base of the crust beneath the root zone in the southern Urals is not a smooth transition but a laterally and vertically heterogeneous structure.

Fig. 11, contains a sketch of the models constrained by the seismic measurements. The final crustal model is the result of the evolution of the orogen after a complex collisional history that started in late Devonian and finished in Triassic times. The validation of any of the two end member models or to constrain any model in between requires a tomographic experiment and multidisciplinary study which is not the scope of this paper. Such a study should integrate data from different disciplines in earth sciences surface geology, geochronology, geochemistry, with geophysics to provide constraints on the possible evolution of the orogen.

6 CONCLUSIONS

Synthetic seismic modelling is an important tool to decide among different possible structures and forming processes of the lower most

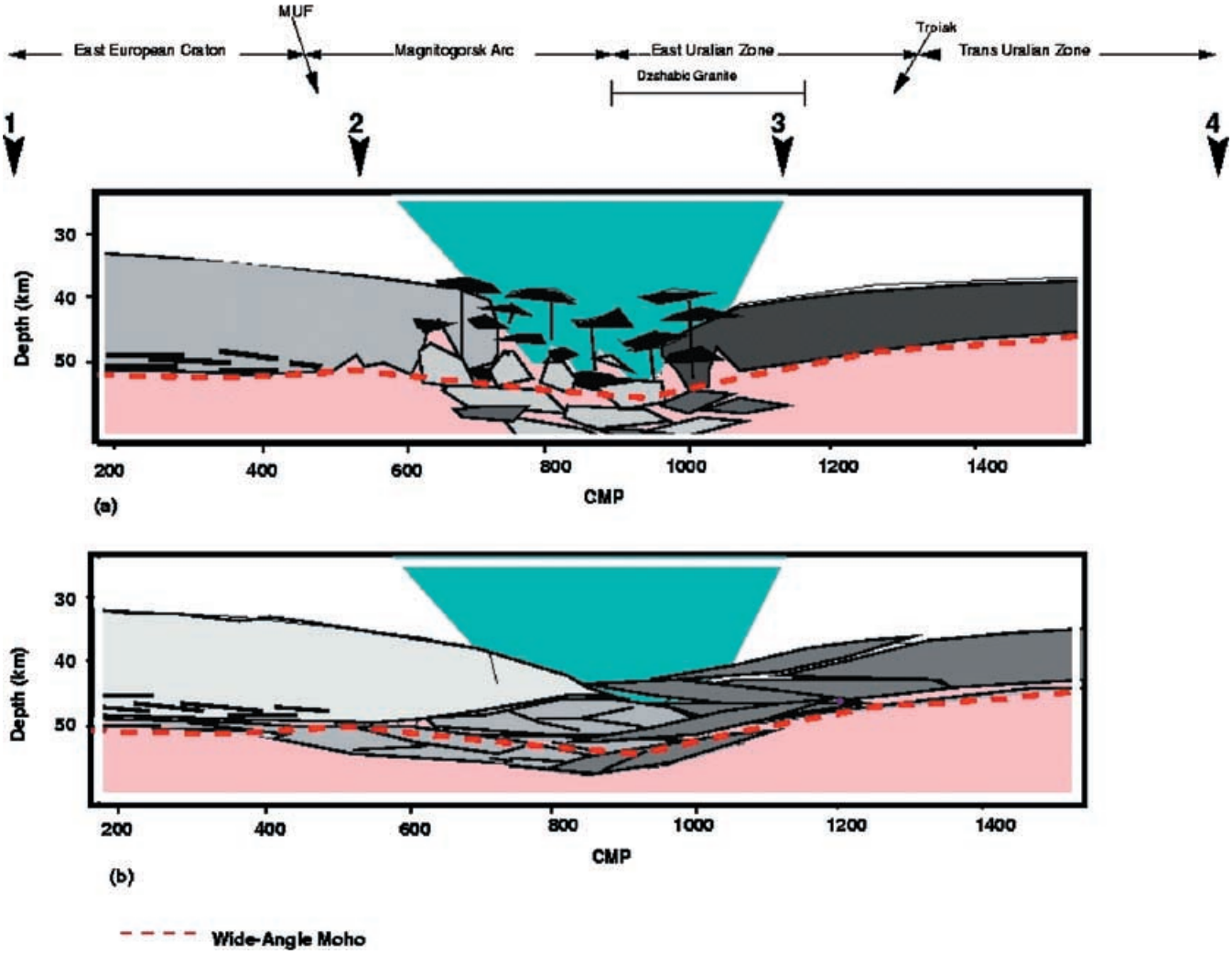

Figure 11. Sketch of possible laterally heterogeneous models for the root zone beneath the southern Urals. The models are mainly characterized by lateral and vertical variations in the physical properties. The deep crust in (a) is a result of magmatic processes (black bodies indicate the intrusions). The gray blocks beneath the Moho (red discontinuous line) denote the possible sources of the Magma. Model (b) illustrates a metamorphic phase change due to upward migration of an eclogitic front. The crustal pieces beneath the Moho would correspond to a mixture of eclogitized crust and mantle. The different domains indicate different degrees of eclogitization. The Magnitogorsk Arc and the East Uralian Zone domain are denoted in blue. The X axis CMP corresponds to the CMP in Figs 2, 3 and 5. The surface geology is sketched on top. The light grey to the west represent the lower crust of the East European Craton and the dark grey to the east represents the lower crust of the Trans-Uralian zone.

crust and Moho. The wide-angle sections, the vertical and horizontal component recordings, and the fan shot gathers imaged arcuate events in the deep crust beneath the root zone of the Urals orogenic belt. The Moho beneath the root zone does not provide a normal incidence *PmP* reflection while it provides a high *PmP* amplitude at far offsets from 75 to 250 km. The *PmP* is also characterized by 1–2 s long coda. The wide-angle shots 1 and 4 recorded at offsets beyond 225 km show a P^*n characterized by relatively high frequencies. 1-D synthetic seismic modelling with a reflectivity algorithm reveals that gradient transitional models do not generate a relevant P^*n phase. A layered structure with alternating fast and low velocities is consistent with the coda of the *PmP* and the P^*n identified in shots 1 and 4. A layered crust–mantle transition is not consistent with the normal incidence CDP images. A 6 km thick, laterally and vertically heterogeneous crust–mantle transition properly simulates the seismic signature at all offsets. The heterogeneous structure can be achieved by laterally discontinuous layers (boudins) with a horizontal correlation length of 600 to 1000 m or by a Moho with and irregular topography on the scale of 5 km. These two models can represent different crustal re-equilibration mechanism one characterized by magmatism and a second which feature metamorphic processes. Finally this studies reveals that until full waveform inversion becomes a viable technique the only sensible approach to get a blurred image of deep targets is by qualitative analysis of the seismic waveforms of the reflected and refracted phases.

ACKNOWLEDGMENTS

This research was funded under the Training and Mobility programme of the European Community under contract URO ERBFMRXCT 960009. This work was carried out in association with the EUROPROBE Uralides Project. Funding was provided by the Comisi'on Interministerial de Ciencia y Technolog'ia (CICYT, Spain) grant PB 97-1141; Generalitat de Catalunya (CIRIT) grant

1999 SGR 00208. This manuscript benefited from the comments by J. Ansorge and from an anonymous reviewer. We also like to acknowledge the effort of the crew members from the GFZ and CSIC-IJA without them these data would not have been acquired.

REFERENCES

Ayarza, P., Brown, D., Alvarez-Marrón, J. & Juhlin, C., 2000. Contrasting tectonic history of the arc-continent suture in the Southern and Middle Urals: implications for evolution of the orogen, *J. geol. Soc. Lond.,* **157,** 1065–1076.

Baird, D., Knapp, J., Steer, D., Brown, L.D. & Nelson, K., 1995. Upper-mantle reflectivity beneath the Williston Basin, phase-change Moho and the orogin of intracratonic basins, *Geology,* **431–434**.

Balling, N., 2000. Deep Seismic reflection evidence for ancient subduction and collision zones within the continental lithosphere of NW Europe, *Tectonophysics,* **329,** 269–300.

Berzin, R., Oncken, O., Knapp, J.H., Pérez-Estaún, A., Hismatulin, T., Yunusov, N. & Lipilin, A., 1996. Orogenic evolution of the Ural Mountains: Results from an integrated seismic experiment, *Science,* **274,** 220–221.

Brown, L.D., 1991. A new map of crustal terraines in the United States from COCORP deep seismic reflection profiling, *Geophys. J. Int.,* **103,** 3–13.

Brown, D., Puchkov, V., Alvarez-Marrón, J. & Pérez-Estaún, A., 1996. The structural architecture of the footwall to the Main Uralinan Fault, southern Urals, *Earth Sci. Rev.,* **40,** 125–147.

Brown, D., Alvarez-Marrón, J., Pérez-Estaún, A., Gorozhanina, Y., Barysghev, V. & Puchkov, V., 1997. Geometric and kinematic evolution of the foreland thrust and fold belt in the southern Urals, *Tectonics,* **16,** 551–562.

Brown, D., Juhlin, C., Alvarez-Marrón, J., Pérez-Estaún, A. & Oslianski, A., 1998. Crustal-scale structure and evolution of an arc-continent collision zone in the southern Urals, *Tectonics,* **16,** 551–562.

Carbonell, R. *et al.*, 1996. Crustal root beneath the Urals: Wide-angle seismic evidence, *Science,* **274,** 222–223.

Carbonell, R., Lecerf, D., Itzin, M., Gallart, J. & Brown, D., 1998. Mapping the Moho beneath the southern Urals with wide-angle reflections, *Geophys. Res. Lett.,* **25,** 4229–4232.

Carbonell, R., Gallart, J., Pérez-Estaún, A., Diaz, J., Kashubin, S.N., Mechie, J., Wenzel, F. & Knapp, J., 2000. Seismic wide-angle constraints on the crust of the southern Urals, *J. geophys. Res.,* **105,** 13 755–13 777.

Christensen, N. & Mooney, W., 1995. Seismic velocity structure and composition of the continental crust: A global view, *J. geophys. Res.,* **100,** 9761–9788.

Dainty, A.M. & Schultz, C.A., 1995. Crustal reflections and the nature of regional P coda, *Bull. seism. Soc. Am.,* **85,** 851–858.

Deemer, S. & Hurich, C., 1994. The reflectivity of magmatic underplating using layerd mafic intrusion analog, *Tectonophysics,* **232,** 239–256.

Echtler, H.P. *et al*., 1996. Preserved collisional crustal structure of the southern Urals revealed by Vibroseis profiling, *Science,* **274,** 224–226.

Egorkin, A.V. & Mikhaltsev, A.V., 1990. The results of seismic investigations along geotraverses, in *Superdeep Continental Drilling and the Deep Geophysical Dounding*, pp. 111–119, eds Fuchs, K., Kozlovsky, Ye.A., Kristsov, A.I. & Zoback, M.D., Spinger-Verlag, Heidelberg.

Enderle, U., Tittgemeyer, M., Itzin, M., Prodehl, C. & Fuchs, K., 1997. Scales of structure in the lithosphere—images of processes, *Soviet Geol. Geophys.,* **275,** 165–198.

Fershtater, G.B., Montero, P., Borodian, N.S., Pushkarev, E.V., Smirnov, V.N. & Bea, F., 1997. Uralian magmatism: an overview, *Tectonophysics,* **276,** 87–102.

Fountain, D.M., Boundy, T., Austrheim, H. & Rey, P., 1994. Eclogite-facies shear zones: deep crustal reflectors?, *Tectonophysics,* **232,** 411–424.

Fuchs, K. & Müller, G., 1971. Computation of synthetic seismograms with the reflectivity method and comparison with observations, *Geophys. J. R. astro. Soc.,* **23,** 417–433.

Goff, J.A. & Jordan, T.H., 1988. Stochastic modeling of seafloor-morphology: inversion of sea beam data for second-order statistics, *J. geophys. Res.,* **93,** 13 589–13 608.

Hale, L.D. & Thompson, G.A., 1982. The seismic reflection character of the continental Mohorovicic discontinuity, *J. geophys. Res.,* **87,** 4625–4635.

Holliger, K. & Robertsson, J.O.A., 1998. Effects of the shallow subsurface on upper crustal seismic reflection images, *Tectonophysics,* **286,** 161–170.

Ivanov, S.N. & Rusin, A.I., 1986. Model for the evolution of the linear fold belt in the continents: example of the Urals, *Tectonophysics,* **127,** 383–397.

Ivanov, S.N., Perfiliev, A.S., Efimov, A.A., Smirnov, G.A., Necheukhin, V.N. & Fershtater, G.B., 1975. Fundamental features in the structure and evolution of the Urals, *Am. J. Sci.,* **275,** 107–130.

Jarchow, C.M., Thompson, G.A., Catchings, R.D. & Mooney, W.D., 1993. Seismic evidence for active magmatic underplating beneath the Basin and Range Province, western United States, *J. geophys. Res.,* **98,** 22 095–22 108.

Juhlin, C., Kashubin, S., Knapp, J.H., Makovsky, V. & Ryberg, T., 1995. Project. conducts seismic reflection profiling in the Ural Mountains, *EOS, Trans. Am. geophys. Un.,* **76,** p. 19.

Juhlin, C., Bliznetsov, M., Pevzner, L., Hismatulin, T., Rybalka, A. & Glushkov, A.A., 1997. Seismic imaging of reflectors in the SG4 borehole, Middle Urals, Russia, *Tectonophysics,* 1–18.

Kanasewich, E.R., Kelamis, P.G. & Abramovici, F., 1983. Exact seismograms for a point force, *Geophysics,* **48,** 1421–1427.

Kennett, B.L.N., 1983. Seismic Wave Propagation in Stratified media, Cambridge University Press, Cambridge.

Kern, H. & Richter, A., 1981. Temperature derivatives of compressional and shear wave velocities in crustal and mantle rocks at 6 kbar confining pressure, *J. geophys. Res.,* **49,** 47–56.

Knapp, J.H. *et al.*, 1996. Lithosphere-Scale seismic image of the southern Urals from explosion-source reflection profiling, *Science,* **274,** 226–228.

Kumazawa, M., Helmstaedt, H. & Masaki, 1971. Elastic properties of eclogite xenoliths from diatremes of the east Colorado plateau and their implication to the upper mantle structure, *J. geophys. Res.,* **76,** 1231–1247.

Larkin, S.P., Levander, A., Henstock, T.J. & Pullammanappallil, S., 1997. Is the Moho flat? Seismic evidence for a rough crust-mantle interface beneath the northern Basin and Range, *Geology,* **25,** 451–454.

Levander, A. & Holliger, K., 1992. Small-scale heterogeneity and largescale velocity structure of the continental crust, *J. geophys. Res.,* **97,** 8797–8804.

Menke, W.H. & Richards, P.G., 1983. Crust-mantle whispering gallery phase: A deterministic model of teleseismic Pn propagation, *J. geophys. Res.,* **85,** 5416–5422.

Mohorovicić, A., 1910. Das Beben von 8.X.1909. Jahrbuch Meteorol. Obs. Zagreb, *Teil4, Abschn,* **4,** 1–63.

Mooney, W. & Meissner, R., 1992. Multi-genetic origin of crustal reflectivity: a review of seismic reflection profiling of the continental lower crust and Moho, in *Developments in Geotectonics, 23, Continental Lower crust,* pp. 45–71, eds Fountain, D.M., Arculus, R. & Kay, R.W., Elsevier, Amsterdam.

Morozov, I., Smithson, S.B., Chen, J. & Hollister, L.S., 2001. Generation of new continental crust and terrane accreation in Southern Alaska and Western British Columbia: constraints from P- and S-Wide-Angle Seismic Data (ACCRETE), *Tectonophysics,* **341,** 49–67.

Navilkin, D.V., 1960. Geology of the USSR, a short outline, Pergammon, Oxford.

Nelson, K.D., 1991. A unified hypothesis of craton evolution motivated by recent deep seismic reflection and refraction results, *Geophys. J. Int.,* **105,** 25–35.

Oliver, J., 1982. Probing the structure of deep continental crust, *Science,* **216,** 689–695.

Rudnick, R. & Fountain, D.M., 1995. Nature and composition of the continental crust: A lower crustal perspective, *Rev. Geophys.,* **33,** 267–309.

Ryberg, T., Fuchs, K., Egorkin, V.A. & Solodilov, L., 1995. High-frequency teleseismic Pn wave observations beneath nothern Eurasia, *J. geophys. Res.,* **100,** 18 151–18 163.

Seravkin, I., Kosarev, A.M. & Salikhov, D.N., 1992. Volcanism of the southern Urals, Nauka, Moscow.

Sochacki, J., George, J.H., Ewing, R.E. & Smithson, S.B., 1991. Interface condiditions for acoustic and elastic wave propagation, *Geophysics,* **56,** 168–181.

Sokolov, V., 1992. The structure of the Earth's crust in the Urals, *Geotectonics,* **5,** 3–19.

Steer, D., Knapp, J., Brown, L.D., Echtler, H.P., Brown, D. & Berzin, R., 1998a. Deep Structure of the continental lithosphere in an unextended orogen: explosive source seismic reflection profile across the Urals (URSEIS 1995), *Tectonics,* **17,** 143–157.

Steer, D., Knapp, J. & Brown, L.D., 1998b. Super-deep reflection profiling: exploring the continental mantle lid, *Tetonophysics,* **286,** 111–121.

Thouvenot, F., Kashubin, S.N., Poupinet, G., ad T.V. Kashubina, V.V.M., Matte, P. & Jenatton, L., 1995. The roots of the Urals: evidence from wide-angle reflection seismics, *Tectonophysics,* **250,** 1–13.

Tittgemeyer, M., Wenzel, F., Fuchs, K. & Ryberg, T., 1996. Wave propagation in a multiple scattering upper mantle—observations and modeling, *Geophys. J. Int.,* **127,** 492–502.

Zonenshain, L.P., Korinevsky, V.G., Kazmin, V.G., Pechersky, D.M., Khain, V.V. & Mateveenkov, V.V., 1984. Plate tectonic model of the south Urals development, *Tetonophysics,* **109,** 95–135.

Zonenshain, L.P., Kuzmin, M.I. & Natapov, L.M., 1990. Geology of the USSR: A plate-tectonic synthesis, in *Uralian Foldbelt, Geodynamics series, Vol. 21,* pp. 27–54, ed. Page, B.M., Am. Geophys. Union, Washington, D.C.